



ELSEVIER

Magnetic Resonance Imaging 20 (2002) 95–104

MAGNETIC  
RESONANCE  
IMAGING

# Analysis of wave patterns in MR elastography of skeletal muscle using coupled harmonic oscillator simulations

Ingolf Sack<sup>a,\*</sup>, Johannes Bernarding<sup>a,b</sup>, Jürgen Braun<sup>a</sup>

<sup>a</sup>Department of Medical Informatics, Biometry and Epidemiology, University Hospital Benjamin Franklin, 12200 Berlin, Germany

<sup>b</sup>Department of Radiology, University Hospital Benjamin Franklin, 12200 Berlin, Germany

Received 28 October 2001; accepted 14 January 2002

## Abstract

The ability to study muscle elasticity *in vivo* would be of great clinical interest. Magnetic resonance elastography (MRE) has the potential to quantify noninvasively the distribution of the shear modulus in muscle tissue. Elasticity information may be derived by extracting frequencies from the wave patterns of phase-contrast MRE images. In a new approach, MRE wave patterns were reconstructed using 3D coupled harmonic oscillator calculations (CHO). To analyze *in vivo* MRE measurements of the biceps brachii of healthy volunteers, different anisotropic fibrous structures for the couplings between the muscle elements have to be assumed. V-shaped wave patterns as observed when excitation was applied on the tendon were reproduced by a model, where in a central band of stiff fascicles wave propagation was about twice as fast as that in surrounding tissue. Planar waves were observed for excitation near the muscle surface. They could be reconstructed by assuming a simultaneous wave excitation of all muscle fibers, where fibers along the main muscle axis were coupled more strongly than those perpendicular to the axis. The results show that CHO calculations provide a fast and reliable method for incorporating anatomical information of the investigated tissue in the reconstruction of complex wave patterns. © 2002 Elsevier Science Inc. All rights reserved.

**Keywords:** *In vivo* MR elastography; Skeletal muscle; Biceps brachii; 3D coupled harmonic oscillators

## 1. Introduction

Tissue elasticity *in vivo* may differ strongly from the elasticity of excised tissue due to variations in hydrostatic pressure or biomechanical mechanisms such as muscle tension [1,2]. The qualitative correlation of function and elasticity appears most obvious in the case of skeletal muscle, where manual palpation has shown that maintaining load increases the muscle stiffness [3]. Surprisingly, only a few studies have been performed to elucidate quantitatively the elasticity of skeletal muscle tissue *in vivo* [4–6]. This may be due to the limited number of noninvasive techniques that allow the distribution of elasticity within a muscle to be monitored. Additionally, the easy and straightforward analysis of elastographic data is often hampered by the complex structure of skeletal muscle tissue that results in complex elastographic data [7].

In recent years, elastographic techniques such as ultra-

sound (US) [8–10] or magnetic resonance imaging (MRI) [11–15] have been developed that combine noninvasive imaging methods with a static or dynamic application of stress to the tissue. *In vivo* studies of skeletal muscle were performed using dynamic elastography of the quadriceps muscle at excitation frequencies between 30 and 120 Hz while maintaining different loads [5]. Experiments at the biceps brachii were achieved by dynamic MR elastography (MRE) applying 150 Hz acoustic frequency [6].

In contrast to ultrasound elastography, MRE enables the entire muscle to be studied and no limitations in penetration depth and maximum resolvable field of view are imposed. To extract elasticity information from MRE phase images, a local frequency estimation may be used [16,17]. Other approaches include the solution of complex tensor equations [18–22]. For isotropic Hookean materials, the shear modulus  $\mu$  can be related directly to the shear wave speed  $c$  by

$$\mu = c^2\rho \quad (1)$$

where  $\rho$  is the tissue density, which was found to be 1100 kg/m<sup>3</sup> for muscle tissue in the literature [6]. Following the terminology of [23], the shear modulus at a given frequency

\* Corresponding author. Tel.: +1-49-30-8445-4506; fax: +1-49-30-8445-4510.

E-mail address: i.sack@medizin.fu-berlin.de (I. Sack).

is henceforth called shear stiffness. Eq. (1) holds for reconstructing the elasticity of skeletal muscle if it is assumed that muscle tissue behaves locally isotropically under dynamic stress [23,24].

In the present study, different experimental observations of MRE images of the biceps brachii of two volunteers are reconstructed by assuming that the muscle fibers may be described by a set of discrete oscillating elements. These elements are arranged in a 3D grid and coupled anisotropically by terms of local wave speeds [25,26]. A corresponding wave equation for the coupled harmonic oscillators (CHO) is then analytically solved for the steady state condition. Calculated wave patterns are fitted to experimental data employing an interactive iterative refinement of the coupling matrix. Additional position-dependent parameters include the attenuation and the transfer of the applied force into the muscle. A previously described 2D CHO approach was extended in the present study to three dimensions.

Experimental observations that reveal different wave patterns depending on how the muscle is excited indicate the need for methods that take into account both muscle properties and excitation parameters for the determination of muscle elasticities. CHO simulations provide the potential to couple single muscle fiber elements with different coupling constants and to incorporate spatially dependent damping and excitation effects, to enable the reconstruction of single wave pattern MRE images.

The goal of this study was the acquisition of experimental wave images under different excitation conditions and the simulation with 2D and 3D CHO calculations. Image reconstruction using the CHO approach was based on two models of anisotropic local couplings. Both models served for fitting different experimental set-ups. Although the results do not allow a final deduction about the physiology of skeletal muscle tissue, the models may aid in understanding the appearance of experimentally observed shear wave patterns in MR elastography.

## 2. Methods

### 2.1. In vivo elasticity measurements

Data were acquired with a standard extremity coil at 1.5 T (Siemens Vision, Germany). Tissue displacement induced by acoustic waves was detected with a modified gradient echo sequence. Trapezoid-shaped motion-encoding gradients, which could be applied in any orientation, sensitized the sequence for probe displacement in the respective direction. Two healthy volunteers were examined in accordance with the board of ethics. The right arm was positioned horizontally. As excitation unit, an actuator coil was used that was fixed to one end of a carbon fiber plate (18 cm long and 2 cm wide), which was fixed to a z-shaped stanchion. A wooden tenon, 4 cm in length, was fixed to the second end of the plate; using Velcro tape, this was then attached to the

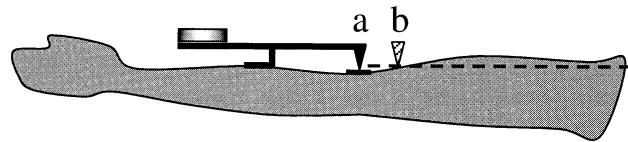


Fig. 1. Experimental setup; the dashed line indicates the approximate slice position of all experiments; a: excitation at the tendon; b: excitation at the distal end of the muscle.

arm either above the distal biceps tendon (Fig. 1a) or within the distal boundary of the muscle (Fig. 1b). A thin spacer ( $0.3 \times 1.5 \times 2$  cm) was inserted between tendon and skin to distribute the pressure more evenly. The design of the excitation unit enabled variable positioning and prevented artifacts by keeping the actuator coil outside the acquisition coil. The excitation plate moved in up- and downward direction. From the resulting spherical waves, solely the shear motion perpendicular to the acquisition plane was encoded corresponding to the direction of the motion-sensitizing gradient. The mechanical excitation profile comprised 7 wave cycles with an excitation frequency  $\omega/2\pi$  of 200 Hz. The mechanical excitation was triggered 25 ms before encoding the particle displacement with two synchronized gradient cycles. The acquisition matrix size was  $256 \times 128$  pixels with a  $320 \times 160$  cm FOV (TR = 60 ms and TE = 12 ms). Two images with inverse shear wave amplitude were recorded in one experiment to allow the subtraction of corresponding phase images. The overall experimental time for recording two phase images was 14 s.

### 2.2. 3D coupled harmonic oscillator calculations

As described recently [25], experimental MRE wave images can be reconstructed by solving a forced wave equation for a set of coupled harmonic oscillators (CHO). To study wave images of skeletal muscle, this approach was extended to a 3-dimensional description, leading to the following wave equation for the displacement  $u$  as a function of the spatial coordinates  $x$ ,  $y$ ,  $z$  and its time dependency  $t$ :

$$\begin{aligned} c(x, y, z)^2 \Delta u(x, y, z, t) - \frac{\partial^2}{\partial t^2} u(x, y, z, t) \\ - \lambda(x, y, z) \frac{\partial}{\partial t} u(x, y, z, t) \\ = F(x, y, z, t), \end{aligned} \quad (2)$$

where  $\Delta$  is the three dimensional Laplace operator.  $c(x, y, z)$  describes the wave velocity,  $\lambda(x, y, z)$  models the local damping of the oscillations, and  $F(x, y, z, t)$  the position-dependent external driving force. Similar to [25], Eq. (2) was simplified by spatial discretization of  $u(x, y, z, t)$  where the indices were chosen to coincide with the discrete pixel resolution of the experimental wave images.

The interaction between the oscillators is modeled by a

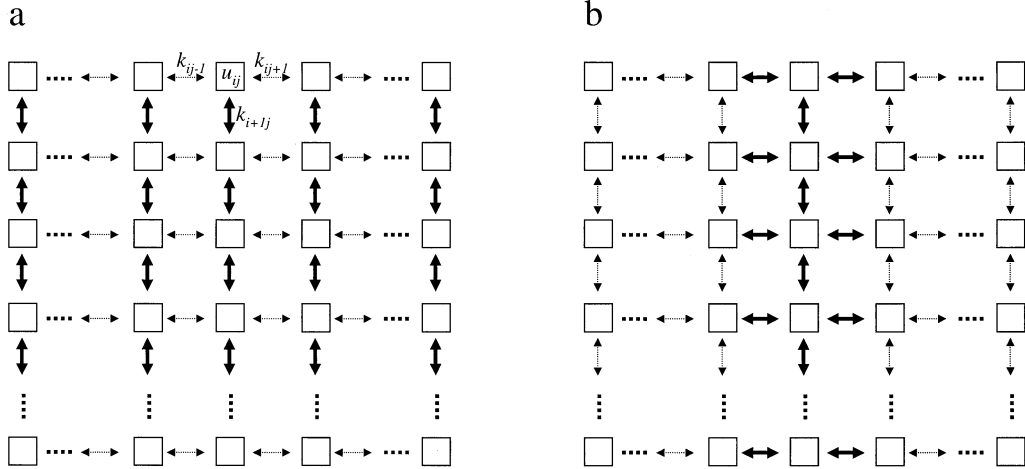


Fig. 2. 2D schemes of the orthogonal arrays of the coupling constants  $k_{ij}$  (arrows) and the oscillators  $u_{ij}$  (boxes). (a) Fiber model: The bold arrows indicate strong longitudinal couplings  $k_l$ , while dashed arrows symbolize weaker transversal interactions  $k_t$ ; as an example, an arbitrary oscillator  $u_{ij}$  with surrounding couplings is depicted. (b) Band model: Bold arrows determine the band with higher wave velocity ( $k_{\max}$ ) while dashed arrows indicate weaker couplings ( $k_{\min}$ ).

grid of coupling constants in  $x$ -,  $y$ -, and  $z$ -direction. Considering only orthogonal nearest-neighbor interactions results in two coupling constants per interior oscillator for each dimension. The coupling constants  $k_{ijk}$  are expressed in frequency units equivalent to terms of wave speeds at a given oscillator distance. It is convenient to describe oscillators and coupling constants in a unified matrix as indicated for the 2D case in Fig. 2a. With this notation, the discrete form of Eq. (2) can be written as

$$\begin{aligned}
 & \frac{d^2}{dt^2} u_{ijk}(t) + \lambda_{ijk} \frac{d}{dt} u_{ijk}(t) + k_{ijk-1}(u_{ijk}(t) \\
 & - u_{ijk-2}(t)) + k_{ijk+1}(u_{ijk}(t) - u_{ijk+2}(t)) \\
 & + k_{ij-1k}(u_{ijk}(t) - u_{ij-2k}(t)) + k_{ij+1k}(u_{ijk}(t) \\
 & - u_{ij+2k}(t)) + k_{i-1jk}(u_{ijk}(t) - u_{i-2jk}(t)) \\
 & + k_{i+1jk}(u_{ijk}(t) - u_{i+2jk}(t)) \\
 & = F_{ijk}(t)
 \end{aligned} \quad (3)$$

where odd indices  $i = 1, 3, \dots, L$ ,  $j = 1, 3, \dots, M$ , and  $k = 1, 3, \dots, N$  encode for the oscillators  $u_{ijk}$ ,  $\lambda_{ijk}$ , and  $F_{ijk}$ , while coupling constants  $k_{ijk}$  are characterized by one even index that changes with the spatial direction (Fig. 2a).  $L$ ,  $M$ , and  $N$  are determined from the number of rows ( $l$ ), columns ( $m$ ), and slices ( $n$ ) of the image matrix with  $L = 2l - 1$ ,  $M = 2m - 1$ , and  $N = 2n - 1$ . Rearranging the oscillators  $u_{ijk}$  and the applied forces  $F_{ijk}$  as column vectors ( $\mathbf{u}$ ,  $\mathbf{F}$ ), the  $\lambda_{ijk}$  as diagonal elements of a square matrix that otherwise contains zeros, and the coupling constants as a coupling matrix  $\mathbf{W}$  similar to [25], Eq. (3) can be written in matrix form as:

$$\frac{d^2}{dt^2} \mathbf{u}(t) + \Gamma \frac{d}{dt} \mathbf{u}(t) + \mathbf{W} \mathbf{u} = \mathbf{F}(t) \quad (4)$$

For CHO simulations Eq. (4) is analytically solved for the steady state, i.e.  $\Gamma t \gg 1$  [25] when all eigen oscillations are damped off and the system oscillates with the frequency  $\omega$  of the excitation force  $\mathbf{F} = \mathbf{F}_0 \cos(\omega t + \varphi_0)$ . If the motion encoding of the MRE acquisition sequence is applied with the same frequency as the excitation  $\mathbf{F}$  occurs, a stroboscopic, quasi time-independent image with a phase shift  $\varphi_0$  results. After solving Eq. (4), the displacement vector  $\mathbf{u}(\varphi_0)$  is rearranged to the initial 3D array of oscillators.

In addition to a homogeneous damping over the whole object, a position-dependent damping was introduced to reproduce the experimental observation that no reflection was detected at muscle boundaries. The maximum attenuation is restricted by the forced harmonic oscillator equation  $\boldsymbol{\omega}_1^2 = \mathbf{W} - \Gamma^2/4$ , with  $\boldsymbol{\omega}_1$  as term for the eigen oscillations being always equal or greater than zero [25]. This treatment of spatial boundaries in CHO simulations may lead to smaller wave amplitudes than observed in the experiment. To improve visualization, amplitudes of  $\mathbf{u}$  are scaled relative to the amplitudes of the driving force and the applied position-dependent damping. This is justified as only local wavelengths are used for the image analysis.

### 2.3. Models for shear wave propagation in muscle tissue

To reconstruct experimentally observed wave patterns of skeletal muscle, both the coupling model  $k_{ijk}$  and the applied force scheme  $F_{ijk}$  were varied. It was assumed that the anisotropic structure of skeletal muscle will lead to an anisotropic distribution of elasticity. The fibrous structure of a human brachial biceps muscle is visible macroscopically as fascicles, which are subdivided into primary fascicles comprising less than 100 fibers with a mean diameter of 50–70  $\mu\text{m}$  for an adult man [3]. Since the fascicles are aligned along the main axis of the muscle, two elasticity models for MRE wave simulations were analyzed: (i) the

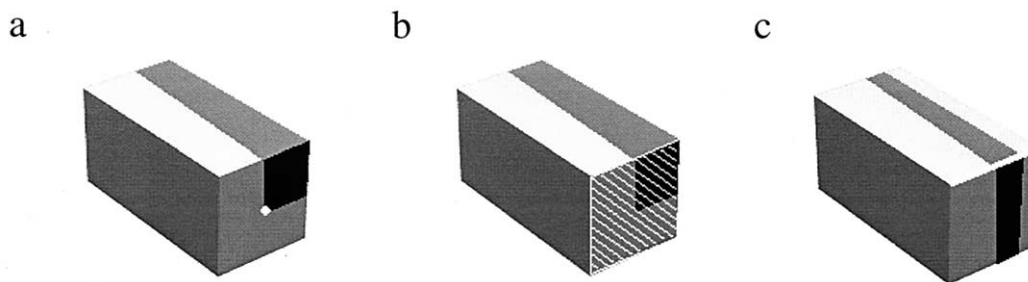


Fig. 3. Excitation schemes for 3D CHO simulations. (a) point-wise excitation in the middle of the first vertical slice, (b) planar excitation of the entire vertical slice, (c) surface-bar excitation at the upper frontal edge. The dark parts of the cuboids symbolize the symmetry-relevant parts of the wave matrix, which have been calculated. Rotation, mirroring, and translation leads to the full matrix.

fiber model: based on observations that acoustic waves travel faster along rather than perpendicular to the fibers of skeletal muscle [5,27], elasticities parallel to the muscle axis were assumed to be higher than those perpendicular to the muscle axis; (ii) the band model: within the central region aligned with the main muscle axis, the homogeneously distributed elasticities are assumed to be higher than in the peripheral region.

The couplings  $k_{ijk}$  are therefore differentiated into longitudinal ( $k_l$ ) couplings with even indices in  $x$ -direction ( $i$ ) and transversal couplings ( $k_t$ ) with even indices in both  $y$ - ( $j$ ) and  $z$ -directions ( $k$ ):

$$k_l = k_{2,4,\dots,L-1;1,3,\dots,M;1,3,\dots,N} \quad (5)$$

$$k_t = k_{1,3,\dots,L;2,4,\dots,M-1;1,3,\dots,N}$$

$$= k_{1,3,\dots,L;1,3,\dots,M;2,4,\dots,N-1}$$

with  $k_l \gg k_t$  (Fig. 2a). The transverse coupling in  $z$ -direction was set equal to  $k_t$  in  $y$ -direction, yielding an axial symmetrical muscle model, where the principal axis (defined by  $k_l$ ) is aligned with the biceps axis.

The band model was deduced from the assumption that a central bundle of fascicles between two tendons might experience higher tension compared to peripheral parts (Fig. 2b). This might cause a higher wave velocity in the center of the muscle between the tendons and parallel to the fibers. Anisotropy is introduced by the ratio between high ( $k_{\max}$ ) and low ( $k_{\min}$ ) coupling values and the spatial extension of the stiff band while longitudinal and transversal couplings are equal in each compartment. The horizontal band profile was chosen as simple rectangular function as indicated in Fig. 2b for a 2D slice of  $\mathbf{k}$ .

### 2.3.1. Excitation models

Three models were considered for the harmonic excitation of the biceps: i) point-wise excitation in the middle of the first vertical slice of the image matrix elements where the force is applied ( $F_{1,m/2,n/2} = 1$ ); ii) excitation of this first slice as its whole ( $F_{1,1,\dots,m,1,\dots,n} = 1$ ); and iii) surface-bar excitation at the upper edge of the force matrix ( $F_{1,1,1,\dots,n} = 1$ ) as indicated in Fig. 3a,b,c. All other elements of  $F$  were set to zero. The point-wise excitation (i)

models the case where the acoustic waves are induced into the biceps purely via the tendon. Planar excitation (ii) occurs if the distal boundary of the biceps is excited by the transducer leading to a synchronous displacement of all fascicles at the distal ending of the muscle. The third excitation mode (iii) was deduced from the case that only those fibers are excited that are close to the transducer position at the muscle surface. This case may occur if the transducer imposes only a weak vibration upon the surface of the biceps. For better understanding, the three excitation modes are treated separately although interactions between all three modes may occur in experiments.

### 2.3.2. Numerical methods

To exploit the extremely sparse character of  $\mathbf{W}$  the calculations were performed in a sparse-matrix routine using Matlab (Version 6, R12; Math Works Inc., Natick, MA). Since Eq. (4) was analytically solved, the resulting CHO-wave image is obtained in a single step. Calculation of a 3D matrix with 32 k elements required approximately 10 min (Athlon 1 GHz, 1 Gb working memory). To reduce computational costs,  $\varphi_0$  was set either to  $0^\circ$  or  $180^\circ$  where sine terms of the steady state solution of the wave equation could be discarded [25].

To increase the resolution, only the symmetry-relevant parts of the final 3D-wave matrix were calculated. For both point-wise and planar excitation, a wave matrix having the size of  $l = 80$ ,  $m = n = 20$  was calculated. The result was mirrored or rotated to the final wave matrix of the size  $l = 80$ ,  $m = n = 40$ . For surface-bar excitation, a single wave block of  $l = 80$ ,  $m = 40$ ,  $n = 10$  was calculated in order to ensure a perspective visualization of waves traveling from the upper surface through the whole phantom (see Fig. 3c).

For comparison with the experiment, slices with arbitrary orientations could be positioned within the reconstructed 3D wave images.

### 2.4. Image analysis

The contrast of experimental MRE phase-difference images is proportional to the local tissue displacement. To compare wave lengths of simulated oscillations to experi-

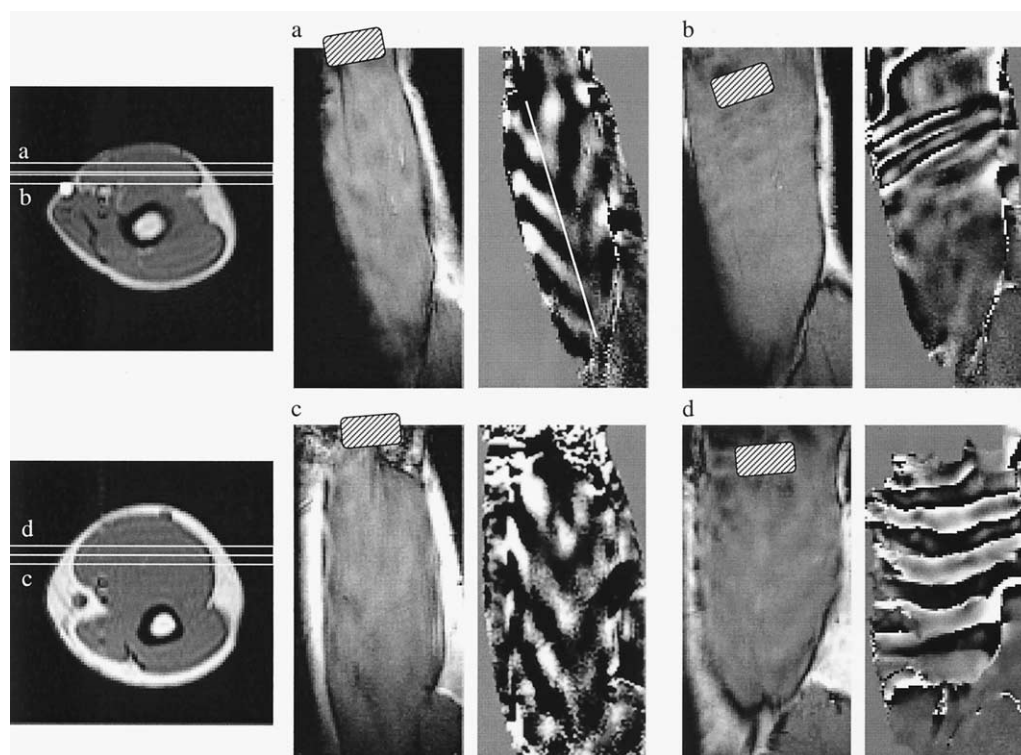


Fig. 4. MRE experiments of the biceps brachii of two volunteers with excitation of 200 Hz (volunteer 1: a/b; volunteer 2: c/d). The gray rectangles depict the position of the excitation unit (cf. Fig. 1a and 1b). The slice positions are indicated by the axial slice profile at the left hand side.

mental data, line profiles were derived from the wave images perpendicular to the wave fronts in the middle of the biceps parallel to the muscle fibers. The wavelengths along directions with similar (isotropic) couplings were converted to wave speeds by multiplication with the excitation frequency of 200 Hz [see Eq. (1)] and then taken as the starting point for the adaption of the coupling constants. To reproduce the shape of the band-model waves, the longitudinal coupling was set equal to the longitudinal coupling in the fiber model, while the transverse coupling was varied. For the band model, the wave speed extracted from the experimental 1D oscillations was applied to the central band. The shape of the wave patterns was varied by changing the ratio  $k_{\min}/k_{\max}$ . To reproduce parallel planar wave fronts, the excitation mode in the simulations was changed from point excitation to planar excitation, while the coupling parameters of the particular model were kept constant. The input parameters for the 2D calculations were deduced from central horizontal slices of previously calculated 3D wave matrices. Other slice positions in the 3D muscle phantom have been used to compare qualitatively the performance of the two coupling models.

### 3. Results

Fig. 4 shows representative MRE images for different excitation modes. It can be clearly seen that the appearance

of MRE wave patterns in muscle depends on the position of the transducer unit. If the waves are induced via the tendon, they are tapered in the direction of wave propagation, appearing as V-shaped waves with an angle of ca.  $55^\circ$  (Fig. 4a, c). In contrast, if the excitation plate is located on the distal surface of the biceps, a larger bunch of fibers is affected instantaneously by the transducer, leading to planar wave fronts perpendicular to the fiber direction (Fig. 4b,d).

This dependency on the excitation mode is reproduced by the 3D calculations (Fig. 5). A pure tendon-wise excitation (Fig. 5a, d) applied to both fiber (Fig. 5, upper row) and band model (Fig. 5, lower row) results in tapered propagating waves. In contrast, pure planar excitation (Fig. 5b, e) yields at first glance planar waves in both models, although their wavelengths appear different. The surface-bar excitation mode (Fig. 5c, f) gives a combination of both tapered and planar propagation patterns.

For comparison with the experiment, representative 2D slices of 3D reconstructed waves are shown in Fig. 6 for tendon and planar excitation of the band model. The orientation of the slices are indicated in Fig. 5d. The comparison of the wave patterns between different slice positions reveals a spatial dependence of the appearing wave patterns. Fig. 6a, representing tendon excitation to the band model, shows no dependency of the wavelength on the slice position, although the shape of the tapered V-waves varies with the enclosed V-angle. In contrast, in the tendon-excited fiber model, the wavelength varies by a factor of about 2 from the

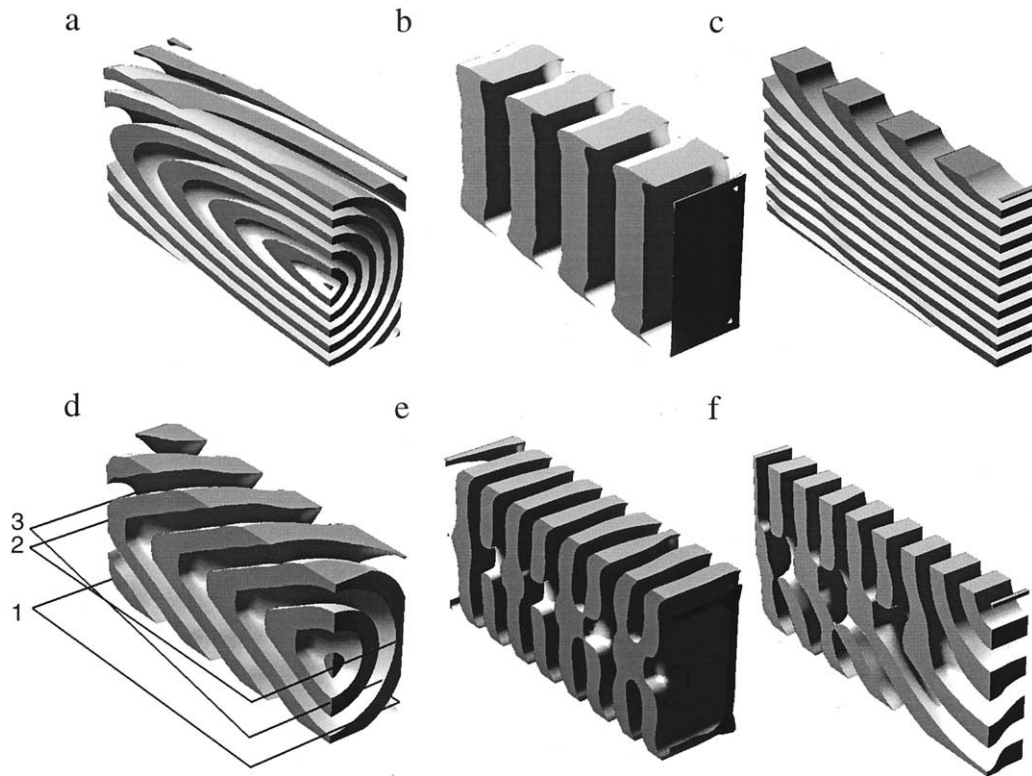


Fig. 5. 3D CHO simulations employing the fiber model (upper row) and the band model (lower row). To improve visualization only half of the full wave matrix  $\mathbf{u}(\varphi_0 = 180^\circ)$  is shown for (a, b, d, e), while in (c, f) only the symmetry-relevant parts of the wave matrix are displayed (cf. Fig. 3). The coupling parameters are  $k_t = 7$  m/s,  $k_r = 1.6$  m/s for the fiber model and  $k_{\max} = 7$  m/s,  $k_{\min} = 3.5$  m/s for the band model. Three representative slice orientations are displayed for the band model (d). The fiber model describes well the position dependency of the excitation and the corresponding transition of wave patterns from ellipsoidal (a) to planar waves (b). Excitation via the surface results in waves that are increasingly coronary oriented with increasing penetration depth (c). The experimental tendon-excited MRE images are best reproduced with the band model as seen in (d). Simulating the other excitation modes results in planar waves with small deviation in the central region of higher stiffness (e, f).

outer edge to the center axis (no 2D slices are shown). It can be seen in Fig. 6a that the V-angle changes between approximately  $100^\circ$  and  $55^\circ$  from slice position 1 to 2. The planar waves of the band model (Fig. 6b) show no dependency of the wavelength on the slice position. Central dis-

tortions of planar wave fronts disappear if slice positions are outside the band (position 1).

Fig. 7 demonstrates the quantitative fit of the experimental wavelengths to a line profile of a central reconstructed 2D wave image where, to a good approximation, the fibers

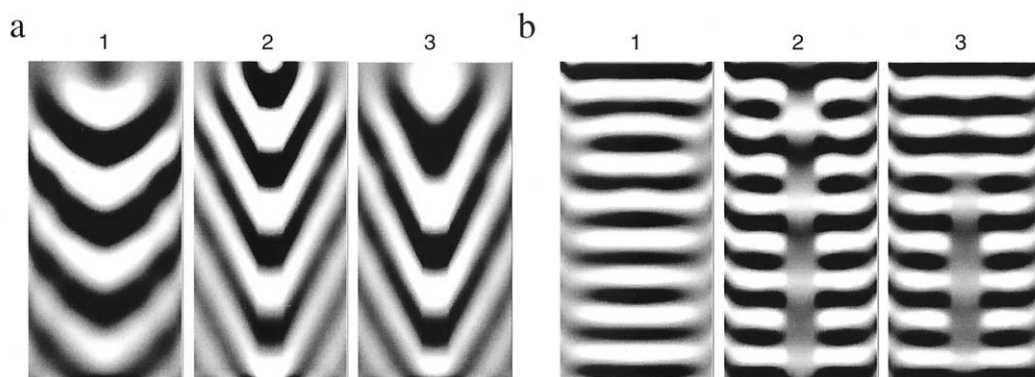


Fig. 6. Representative slices from a 3D CHO calculation of the band model corresponding to Figs. 5d exhibiting a slice close to the surface (1), a central slice (2), and an oblique slice (3). The corresponding wave patterns of the tendon excitation (a) and the planar excitation (b) depict the dependency of the wave pattern on position and tilt of the slices. While in (a) the angle of the V-shaped wave patterns varies, the wave fronts in (b) change from purely planar waves as a result of the central band of higher stiffness and faster wave propagation to planar wave fronts with additional central distortions. For comparison with experimental MRE, see Fig. 4a–d.

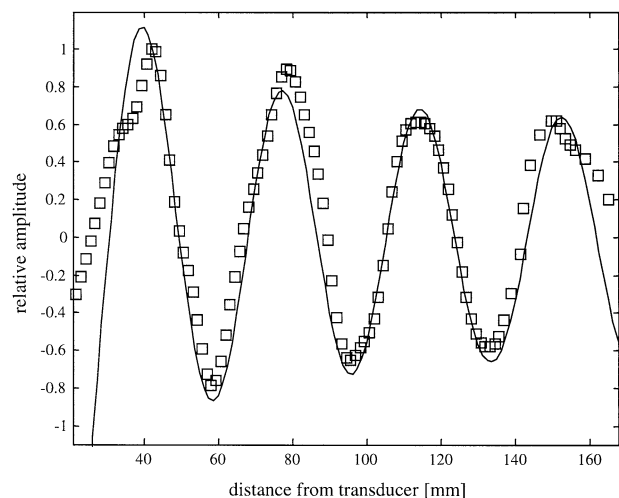


Fig. 7. Experimental signal values (open rectangles) and calculated fit curve (line) of a central 1D profile along the muscle axis (Fig. 4a, indicated as bold white line). The fit based on an isotropic model yielded a wave propagation along the axis of  $7.0 \pm 0.2$  m/s.

can be assumed to be collinear with the muscle axis. Fig. 8 shows the results of a reconstruction of the corresponding slice using a 2D CHO simulation for both coupling models. An isotropic coupling matrix served as reference for both coupling models, i.e.  $k_t = k_l$  and  $k_{\min} = k_{\max}$  for the fiber and the band model, respectively. The coupling was found to be 7.0 m/s by fitting to the experimental profile data of Fig. 7. The wave speed tolerance was estimated to be 0.2 m/s by interactive iteration of the coupling in the isotropic model. The corresponding shear stiffness is calculated to be  $54 \pm 3$  kPa using Eq. (1). For volunteer 2, the muscle elasticity was determined under tendon excitation with a wave propagation speed of  $8.1 \pm 0.3$  m/s to  $72 \pm 5$  kPa shear stiffness. The planar waves in the experimental data of Fig. 4b and 4d were fitted by smaller coupling values. The biceps brachii of volunteer 1 exhibited a planar wave propagation speed of  $4.4 \pm 0.3$  m/s, while  $5.1 \pm 0.5$  m/s for volunteer 2 was found. This corresponds to shear stiffness values of  $21 \pm 3$  kPa and  $29 \pm 6$  kPa.

The effect of increasing anisotropy is illustrated in Fig. 8 (upper row), which shows the fiber model exposed to point excitation. The transverse coupling was varied from 3.2 to 1.6 m/s, while the longitudinal coupling was kept constant at 7.0 m/s. The ellipsoidal wave fronts produced by the fiber model differ from the V-waves of the experiment. Therefore, only a coarse estimation of the anisotropy within the fiber model could be made. Varying the transverse coupling gives a hint about the strength of the transverse wave propagation in experiments. It was estimated that the shear waves propagate approximately 4.5 times faster along the fibers than perpendicular to them, i.e.  $k_t$  would be around 1.6 m/s for volunteer 1 (Fig. 4a) and 1.8 m/s for volunteer 2 (Fig. 4c). Changing to an excitation mode with a planar force reproduces planar parallel wave fronts. For the fiber model, wavelengths of those planar waves coincide with the

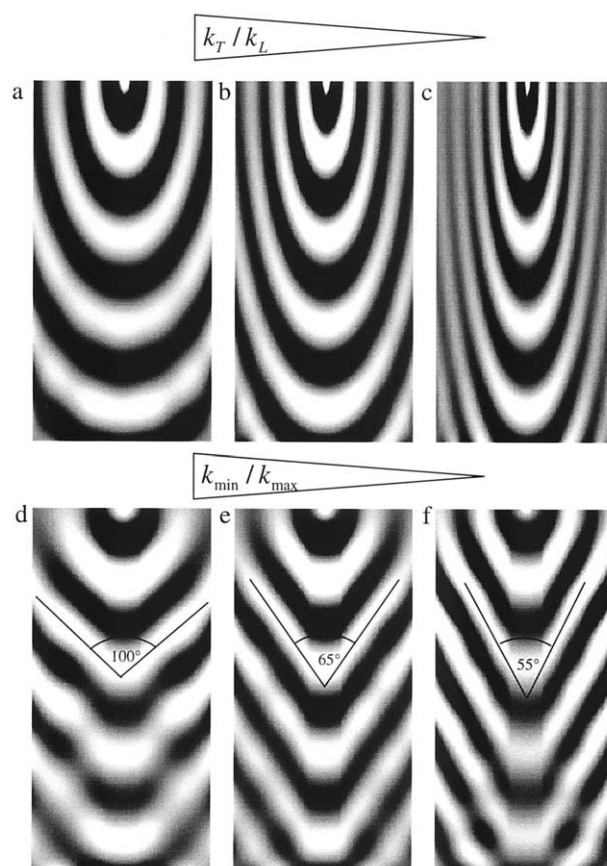


Fig. 8. 2D CHO simulations corresponding to a tendon-excited central slice of the 3D calculations of Fig. 6. Wave patterns for fiber model (upper row) and band model (lower row). Start value for simulation was the isotropic coupling ( $k_h = 7$  m/s) as extracted from the 1D line profile. This value was applied as longitudinal coupling  $k_t$  to the fiber model and as maximum coupling  $k_{\max}$  for the band model. Increasing anisotropy with  $k_t/k_l$  of 0.45 (a), 0.32 (b), 0.22 (c) causes increasing ellipsoidal character of the wave pattern in the fiber model. Increasing anisotropy in the band model with  $k_{\min}/k_{\max}$  changing from with 0.7 (d), 0.6 (e), 0.5 (f) results in decreasing angles enclosing the V-waves. The blurring in the center is again due to the band of higher stiffness and the faster wave propagation.

wavelengths of the isotropic coupling model, i.e. the transverse coupling under planar excitation has no influence on the appearance of the waves (see Fig. 5b). Thus, by analyzing the experiments of Fig. 4b and 4d using the fiber model, no information about anisotropic couplings can be obtained.

Results applying the band model are shown in Fig. 8 (lower row). Assuming that the profile of the vertical band can be approached by a simple rectangular step function (see Fig. 2b), the ratio  $k_{\min}/k_{\max}$  is the crucial parameter for simulating the V-angle under point excitation. For the calculations in Fig. 8d,e,f the width of the stiff band was set to 15% of the object width. To adjust the V-angle in the wave patterns, only the weak coupling  $k_{\min}$  was varied. Fig. 8d,e,f shows a decreasing  $k_{\min}$  with 5.0, 4.2, and 3.5 m/s. The best fit to the experimental V-angle of  $55^\circ$  was obtained using a ratio  $k_{\min}/k_{\max}$  of 0.5, corresponding to a  $k_{\min}$  of 3.5 m/s. The tolerance of the ratio  $k_{\min}/k_{\max}$  for simulating the ex-

Table 1  
Coupling and elasticity parameters for the simulation of experimental data with the fiber and band models

	Isotropic model		Fiber model				Band model			
	$k_h$ [m/s]	$\mu_h$ [kPa]	$k_t$ [m/s]	$\mu_t$ [kPa]	$k_t$ [m/s]	$\mu_t$ [kPa]	$k_{\max}$ [m/s]	$\mu_{\max}$ [kPa]	$k_{\min}$ [m/s]	$\mu_{\min}$ [kPa]
4a	7.0 (0.2)	54 (3)	7.0* (0.2)	54* (3)	1.6**	2.8**	7.0* (0.2)	54* (3)	3.5 (0.3)	13.5 (2.5)
4b	4.4 (0.3)	21 (3)	4.4* (0.3)	21* (3)	—	—	—	—	4.4* (0.3)	21* (3)
4c	8.1 (0.3)	72 (5)	8.1* (0.3)	72* (5)	1.8**	3.6**	8.1* (0.3)	72* (5)	4.0 (0.4)	18.0 (3.5)
4d	5.1 (0.5)	29 (6)	5.1* (0.5)	29* (6)	—	—	—	—	5.1* (0.5)	29* (6)

\* Values taken from the isotropic model; \*\* Estimated values (no error tolerance is given due to ellipsoidal wave shapes; for further details see text).

perimental V-angle of  $55^\circ$  was estimated with  $\pm 0.05$ . For the experiment shown in Fig. 4c,  $k_{\min}$  was found with 4.0 m/s. The determined coupling ratio results in a shear stiffness  $\mu_{\min}$  of 13.5 and 17.5 kPa for the experiments shown in Fig. 4a,c.

These values were also used for the maximum and minimum coupling values with planar excitation (Fig. 5e). Here, the main wave propagation is governed by the weak coupling, showing that under planar excitation different elasticities are revealed using either the band or the fiber model.

Parameters used for the reconstruction of experimental MRE images are summarized in Table 1.

#### 4. Discussion

The experiments show that MRE can be used to monitor the wave propagation of acoustically induced waves within muscle tissue. At 200 Hz excitation frequency the detected wave patterns depend strongly on the mode of excitation. This is due to the strong anisotropic character of skeletal muscle tissue. A pure image-based analysis of the wave patterns to determine the muscle elasticity may therefore lead to insufficient results. In contrast, CHO-based reconstruction allows the simulation of different models of anisotropy and excitation modes in order to analyze MRE experiments of skeletal muscle. Additionally, choosing arbitrary slice positions within the 3D reconstructed wave images allows the comparison with different experimental slice positions of the in vivo measurements.

The experimental observations of different wave patterns have to be explained: Point excitation of the tendon leads to V-shaped wave fronts, while exciting a greater bunch of fascicles at the distal ending of the muscle yields planar wave fronts perpendicular to the fiber direction. For the latter experimental condition, the phase images show a higher amplitude of planar waves compared to the pointwise excitation across the tendon. This is probably caused by both the proximity of the transducer to the muscle and the number of simultaneously excited fibers.

However, the fully 3D calculation suffers from long computational times. In principle, it should be possible to reconstruct the main features of the wave propagation inside one slice using 2D simulations. In Fig. 5d three slice positions are depicted, which have been used to compare simulations with experimental wave patterns. Due to the rectangular grid of couplings, each horizontal slice (indicated by 1 and 2 in Fig. 5d) exhibits a 2D coupling matrix  $\mathbf{k}_{2D}$  that coincides with the particular 2D part of the 3D couplings of slice  $k$ . To use a 2D scheme for computation also requires the corresponding spatial distribution of force and damping constants. For the tendon-induced and planar excitations (see Fig. 3a,b) the schemes are identical for the central slice of the cuboid (slice 2 with  $k = n/2$ ). As a consequence of the reduction, 3D wave patterns display lower amplitudes due to the exchange of energy in an additional space direction in 3D reconstruction. However, wave patterns that were used only to extract the relevant information remained comparable. As the main focus of this analysis was to reconstruct the shape and number of the wave fronts as a direct expression of the shear stiffness in the object, all quantities that required an iterative adaption of couplings were determined by 2D CHO simulations using the central horizontal slice.

To model the anisotropy, two coupling models were developed. Despite their simplicity, these models resulted in different wave patterns depending on the excitation mode. The fiber model is based on the observation that acoustic waves travel along the fiber direction faster than perpendicular to it. The fiber model explains the change of tapered wave patterns into planar waves depending on the position of the transducer plate. This model reproduces ellipsoidal wave patterns that only partially resemble the tapered V-shape of waves excited via tendon. However, the ellipsoidal wave form permits a qualitative comparison of the wavelength of experimental data, leading to an estimation of the ratio between longitudinal and transversal wave speeds in the biceps brachii. Anisotropy information is lost if all fibers are excited simultaneously at the distal end of the muscle, leading to planar waves.

The second model exploits the fact that different amounts of local intramuscular pressure or a bundle of stronger tensed fascicles parallel to the muscle axis may result in a coupling matrix with a band structure like that displayed in Fig. 2b. This model reproduces the shape of the tapered V-waves (Fig. 4a,c) and allows the fit of the V-angle of the experimental waves with an approximated tolerance of  $\pm 5^\circ$ . To adjust this angle, the ratio of the wave speeds inside and outside the stiff band was varied, leading to an optimum value of the ratio of  $0.5 \pm 0.05$ . Provided that the muscle elasticity is strongly influenced by the tension within the muscle, in the relaxed state a relative homogeneous distribution of tension would be expected on the macroscopic scale of the MRE experiments. On the other hand, as the volunteers reported, it is difficult to maintain a state of total relaxation during the experiment due to the stimulus of induced acoustic waves. This could explain why i) the observed elasticities vary to a certain degree between the experiments, and ii) even in a relaxed muscle some low tension may occur.

However, the band model cannot reproduce parallel wave fronts over the whole object (Fig. 6b). On the other hand, the 3D-wave simulations using point-wise excitation indicate that the band model is more feasible than the fiber model in terms of the wave form and distribution of the wave propagation. The fiber model displays a stronger dependency of the apparent wave length on the slice position. The number of wave fronts increases while traveling through the 3D wave cube from the surface towards the center (approximately from 2 to 4 wave numbers). Such dependence of the wave number on the position of the image plane is found neither in the case of 3D band model simulations nor in the experimental data. In experiments the slice position changed slightly by making small adjustments to the arm position while shifting the transducer. The individual slice position shown in Fig. 4 indicates that the V-waves were recorded with different relative slice positions for volunteers one and two. The relative outer slice position of volunteer one would cause strong ellipsoids up to vertically running wave fronts in the fiber model, while the band model implies solely a larger V-angle compared to volunteer two. Since an identical V-angle was found in both experiments, the band model imposes a smaller ratio  $k_{\min}/k_{\max}$  for volunteer one, in order to fit to the experimental V-angle of  $55^\circ$  at an outer slice position.

For both volunteers, the experimental planar waves exhibit shorter wave lengths compared to the tendon-wise excitations. Also the reconstructed wave velocities of the V-shaped waves were approximately 1.6 times higher than the velocities of the planar waves. While in the fiber model both velocities should be equal, the band model will lead to a difference between planar and V-wave propagation corresponding to the anisotropy factor  $k_{\min}/k_{\max}$ . For the ratio  $k_{\min}/k_{\max} = 0.5$  as found by the simulations, the V-waves will propagate 2 times faster than planar waves. On the other hand, a more elaborate fiber model with shorter but

overlapping fibers will require the inclusion of transversal couplings already for the planar wave propagation. The corresponding coupling matrix would imply a wave propagation corresponding to the mean coupling  $\bar{k}$  between transverse and longitudinal couplings. Such  $\bar{k}$  varies between 4.3 and 4.9 m/s corresponding to averaged elasticities  $\bar{\mu}$  between 26 and 20 kPa for both volunteers (Fig. 4). These values have the same orders of magnitude as previously published results of *in vivo* US and MRE measurements of the biceps brachii [5,6]. However,  $\mu_l$  of the fiber model and  $\mu_{\max}$  of the band model display a larger elasticity than found in [5,6], where an isotropic elasticity value was determined by 1D line profiles of V-shaped wave patterns excited at 150 Hz. The difference to our results may be due to the frequency dependence of the observed shear modulus caused by shear viscosity as our measurements were performed at 200 Hz [23,27]. A partial stimulation by the induced vibrations resulting in changed muscle tension or intramuscular pressure may also lead to differences in the measured elasticity.

The variations in elasticity of approximately 25% between volunteers 1 and 2 are within the range of previous studies [5,6]. Although this variability may render it difficult to compare MRE experiments of different individuals, the sensitivity of MRE to individual relaxation states or muscle strength will make it possible to investigate *in vivo* muscular functions by mapping the stiffness distribution as well as by analyzing the shape of the strain waves in the tissue. Further examinations and more elaborate models combining overlapping fiber structures and smooth tension profiles could extend our knowledge about *in vivo* muscle properties.

## 5. Conclusion

Three dimensional CHO calculations were shown to allow an analysis of complex wave patterns of MRE of skeletal muscle. Depending on the transducer position, *in vivo* experiments of the biceps brachii showed differing wave patterns (V-waves and planar waves). The features could be described with two models of anisotropic wave propagation in the muscle. In the fiber model, the elasticity was attributed to different longitudinal and transversal components. The band model was based on tension dispersion, forming a band of higher wave velocity along the muscle axis. Both models are complementary tools for analyzing the experimental wave images. The shape of V-waves in two and three dimensions is better described by the band model, whereas the fiber model gives a better explanation for the transition from V-waves to planar waves as observed experimentally by shifting the transducer plate from the tendon to the beginning of the biceps. The reconstructed elasticity values varied between the volunteers probably due to slightly different tension of the muscle. The results indi-

cate the potential use of different anisotropy models to gain more insight into the in vivo function of muscle tissue.

## References

- [1] Fung Y. Biomechanics: mechanical properties of living tissue. New York: Springer-Verlag, 1993.
- [2] Sarvazyan AP, Skovoroda AR, Emelianov SY, Fowlkes JB, Pipe JG, Adler RS, Buxton RB, Carson PL. Acoustical imaging. In: Jones JP, editor. New York: Plenum Press, vol. 21, 1995.
- [3] Schmalbruch H. Skeletal muscle. Berlin Heidelberg: Springer-Verlag, 1985.
- [4] Dresner MA, Rose GH, Rossman PJ, Smith JA, Muthupillai R, Ehman RL. Functional MR elastography of human skeletal muscle. Proceedings of the 6th Conference of the International Society Magnetic Resonance Med 1998;463.
- [5] Levinson SF, Shinagawa M, Sato T. Sonoelastic determination of human skeletal muscle elasticity. J Biomechanics 1995;28:1145–54.
- [6] Dresner MA, Rose GH, Rossman PJ, Muthupillai R, Manduca A, Ehman RL. Magnetic resonance elastography of skeletal muscle. J Magn Reson Imaging 2001;13:269–76.
- [7] Gao L, Parker KJ, Lerner RM, Levinson SF. Imaging of the elastic properties of tissue—A review. Ultrasound Med Biol 1996;22:959–77.
- [8] Lerner RM, Huang SR, Parker KJ. “Sonoelasticity” images derived from ultrasound signals in mechanically vibrated tissues. Ultrasound in Med & Biol 1990;16:231–9.
- [9] Parker KJ, Huang SR, Musulin RA, Lerner RM. Tissue response to mechanical vibrations for “sonoelasticity imaging.” Ultrasound in Med & Biol 1990;16:241–6.
- [10] Ophir J, Cespedes I, Ponnekanti H, Yazdi Y, Li X. Elastography: a quantitative method for imaging the elasticity of biological tissues. Ultrasonic Imaging 1991;13:111–34.
- [11] Fowlkes JB, Emelianov SY, Pipe JG, Skovoroda AR, Carson PL, Adler RS, Sarvazyan AP. Magnetic-resonance imaging techniques for detection of elasticity variation. Med Phys 1995;22:1771–8.
- [12] Lewa CJ, de Certaines JD. MR imaging of viscoelastic properties. J Magn Reson Imaging 1995;5:242–4.
- [13] Muthupillai R, Lomas DJ, Rossman PJ, Greenleaf JF, Manduca A, Ehman RL. Magnetic resonance elastography by direct visualization of propagating acoustic strain waves. Science 1995;269:1854–7.
- [14] Plewes DB, Betty I, Urchuk SN, Soutar I. Visualizing tissue compliance with MR imaging. J Magn Reson Imaging 1995;5:733–8.
- [15] Chenevert TL, Skovoroda AR, O'Donnell M, Emelianov SY. Elasticity reconstructive imaging by means of stimulated echo MRI. Magn Reson Med 1998;39:482–90.
- [16] Knutsson H, Westin CJ, Granlund G. Local multiscale frequency and bandwidth estimation. Proceedings of the IEEE International Conference on Image Processing. 1994;1:36–40.
- [17] Manduca A, Muthupillai R, Rossman PJ, Greenleaf JF, Ehman RL. Image processing for magnetic resonance elastography. In: Loew MH, Hanson KM, editors. Proceedings of SPIE's International Symposium Medical Imaging. 1996;2710:616–23.
- [18] Romano AJ, Shirron JJ, Bucaro JA. On the noninvasive determination of material parameters from a knowledge of elastic displacements: Theory and numerical simulation. IEEE Trans Ultrason Ferr 1998;45:751–9.
- [19] Sinkus R, Lorenzen J, Schrader D, Lorenzen M, Dargatz M, Holz D. High-resolution tensor MR elastography for breast tumour detection. Phys Med Biol 2000;45:1649–64.
- [20] Bishop J, Samani A, Sciarretta J, Plewes D. Two-dimensional MR elastography with linear inversion reconstruction: methodology and noise analysis. Phys Med Biol 2000;45:2081–91.
- [21] Oliphant TE, Manduca A, Ehman RL, Greenleaf JF. Complex-valued stiffness reconstruction for magnetic resonance elastography by algebraic inversion of the differential equation. Magn Reson Med 2001;45:299–310.
- [22] Van Houten E, Miga M, Weaver J, Kennedy F, Paulsen K. Three-dimensional subzone-based reconstruction algorithm for MR elastography. Magn Reson Med 2001;45:827–37.
- [23] Kruse SA, Smith JA, Lawrence AJ, Dresner MA, Manduca A, Greenleaf JF, Ehman RL. Tissue characterization using magnetic resonance elastography: preliminary results. Phys Med Biol 2000;45:1579–90.
- [24] Manduca A, Oliphant TE, Dresner MA, Mahowald JL, Kruse SA, Amromin E, Felmlee JP, Greenleaf JF, Ehman RL. Magnetic resonance elastography: non-invasive mapping of tissue elasticity. Medical Image Analysis 2001;5:237–54.
- [25] Braun J, Buntkowsky G, Bernarding J, Tolxdorff T, Sack I. Simulation and analysis of magnetic resonance elastography wave images using coupled harmonic oscillators and Gaussian local frequency estimation. Magn Reson Imaging 2001;19:703–13.
- [26] Sack I, Buntkowsky G, Bernarding J, Tolxdorff T, Braun J. New approach for analyzing magnetic resonance elastography images. Proceedings of SPIE's International Symposium Medical Imaging. San Diego: SPIE. 2001;4320:868–74.
- [27] Smith JA, Muthupillai R, Dresner A, Hulshizer TC, Greenleaf JF, Ehman RL. Tissue characterization using magnetic resonance elastography. Proceedings of the 5th Conference of the International Society Magnetic Resonance Med. 1997. p. 1903.